Impact of an electrode-diaphragm gap on diffusive hydrogen crossover in alkaline water electrolysis

Available online at www.sciencedirect.com

ScienceDirect

journal homepage: www.elsevier.com/locate/he

Impact of an electrode-diaphragm gap on diffusive hydrogen crossover in alkaline water electrolysis

Rodrigo Lira Garcia Barros [a], *Joost T. Kraakman* [a], *Carlijn Sebregts* [a], *John van der Schaaf* [a,b], *Matheus T. de Groot* [a,b,*]

[a] *Department of Chemical Engineering and Chemistry, Sustainable Process Engineering Group, Eindhoven University of Technology, P.O. Box 513, Eindhoven, 5600 MB, the Netherlands*

[b] *Eindhoven Institute for Renewable Energy Systems, Eindhoven University of Technology, PO Box 513, Eindhoven 5600 MB, the Netherlands*

HIGHLIGHTS

- Supersaturation is a major driver for gas crossover in zero-gap electrolysis.
- Supersaturation near the diaphragm surface is influenced by cathode-diaphragm gap.
- Large variations in gas crossover are observed for a zero-gap electrolyzer.

GRAPHICAL ABSTRACT

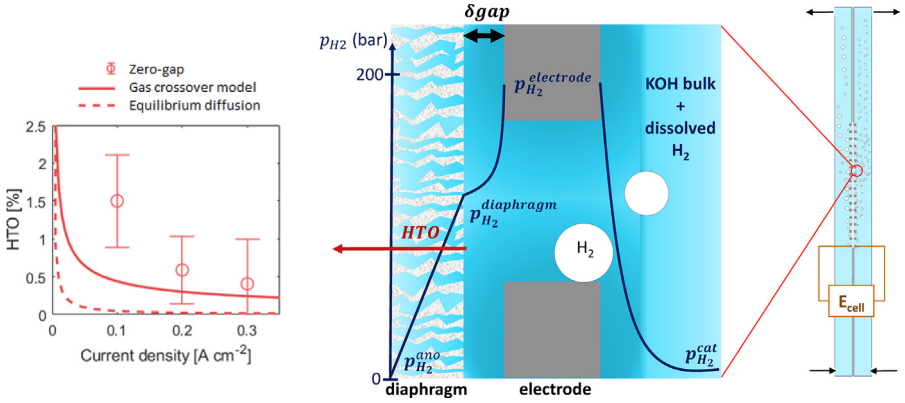

ARTICLE INFO

Article history:
Received 7 August 2023
Received in revised form
22 September 2023
Accepted 26 September 2023
Available online 25 October 2023

Keywords:
Alkaline water electrolysis
Hydrogen crossover
Zero-gap

ABSTRACT

Hydrogen crossover limits the load range of alkaline water electrolyzers, hindering their integration with renewable energy. This study examines the impact of the electrode-diaphragm gap on crossover, focusing on diffusive transport. Both finite-gap and zero-gap designs employing the state-of-the-art Zirfon UTP Perl 500 and UTP 220 diaphragms were investigated at room temperature and with a 12 wt% KOH electrolyte. Experimental results reveal a relatively high crossover for a zero-gap configuration, which corresponds to supersaturation levels at the diaphragm-electrolyte interface of 8–80, with significant fluctuations over time and between experiments due to an imperfect zero-gap design. In contrast, a finite-gap (500 μm) has a significantly smaller crossover, corresponding to supersaturation levels of 2–4. Introducing a cathode gap strongly decreases crossover, unlike an anode gap. Our results suggest that adding a small cathode-gap can significantly

* *Corresponding author*. Department of Chemical Engineering and Chemistry, Sustainable Process Engineering Group, Eindhoven University of Technology, P.O. Box 513, Eindhoven, 5600 MB, the Netherlands.
E-mail address: M.T.d.Groot@tue.nl (M.T. de Groot).

https://doi.org/10.1016/j.ijhydene.2023.09.280

Supersaturation
Electrolyzer design

decrease gas impurity, potentially increase the operating range of alkaline electrolyzers, while maintaining good efficiency.

1. Introduction

Green hydrogen produced via water electrolysis powered by renewable energy sources is expected to play an important role in the energy transition as an energy carrier and feedstock for the chemical industry [1,2]. Based on expected future green hydrogen demand it is projected that terawatts of electrolysis capacity are needed [3]. Of the available water electrolysis technologies alkaline water electrolyzers (AWE) seems particular suitable, since it has less dependence on rare and expensive materials than other techniques [4].

Traditional AWE electrolyzers have a finite-gap design, in which the inter-electrode distance is about 1–3 mm [5]. The use of a zero-gap assembly with a thin diaphragm [6] is considered more attractive for advanced alkaline water electrolysis. It reduces ohmic resistance by minimizing the cathode-anode distance and in this way enables efficient operation at higher current densities. Yet, a thin diaphragm also leads to increased H_2 crossover from the cathodic to anodic compartment. This increased crossover poses a potential risk as it can lead to the formation of an explosive mixture, if 4 vol% of H_2 in O_2 is reached [6]. The volume fraction of hydrogen in oxygen (HTO) is important for the load flexibility of an alkaline water electrolyzer, as HTO increases with decreasing current density due to lower oxygen production. The minimum load of the electrolyzer, which is the lowest current density at which an electrolyzer can be safely operated, is usually determined by the current density at which the HTO reaches 1.6% [6]. The typical minimum load for alkaline electrolyzers varies from 10 to 40% [7], and also depends on the nominal current density and the operating pressure. A low minimum load is especially relevant for electrolyzers operated based on variable renewable electricity [8] and therefore there is a desire to decrease it.

Hydrogen crossover through the diaphragm can be driven by diffusion, convection and electrolyte mixing [6,9–12]. For electrolyzers operated at well-balanced pressures and industrial flow rates, diffusion is believed to be the main contributor to H_2 crossover [6,13]. Studies where electrolyte mixing has been observed to be the main driver for crossover typically employ significantly higher flow rates than industrial alkaline electrolyzers. In the work of Trinke et al. [11] a flow rate of 21 L h^{-1} is used for a current of up to 70 A, which corresponds to 0.3 L h^{-1} A^{-1}. In contrast, a typical commercial alkaline electrolyzer has a flow rate of ~550 L h^{-1} for 10 Nm^3 h^{-1} [14]. The latter corresponds to a current normalized flow rate of 0.023 L h^{-1} A^{-1}.

Diffusion is driven by a high local-supersaturated H_2 pressure at the diaphragm interface. Yet, the understanding of this supersaturation at the diaphragm interface in a zero-gap is still poor, since it is a complex interplay between the hydrogen generation at the electrode surface, hydrogen bubble formation [15] and mass transport of dissolved hydrogen away from the electrode. The schematic representation in Fig. 1 shows the H_2 partial pressure profile in a close to zero-gap electrolyzer during electrolysis. Here, the hydrogen pressure at the diaphragm interface ($p_{H_2}^{diaphragm}$) is expected to be in between the pressure at the electrode surface ($p_{H_2}^{electrode}$), where the supersaturation is highest, and the bulk catholyte, where the supersaturation will be low ($p_{H_2}^{cat}$).

Supersaturation is defined as the ratio between the concentration of the dissolved gas and the equilibrium solubility of the gas [15,16]. The local supersaturation in the immediate vicinity of a gas-evolving electrodes can be more than hundred-fold the hydrogen solubility [15–18]. Shibata [16] reported supersaturation levels of up to 160 for a platinum cathode in 1.0 M H_2SO_4 electrolyte at 25 °C. No data regarding the supersaturation levels of hydrogen gas at the electrode surface was found in concentrated alkaline medium. Nonetheless, a number of authors have suggested that the supersaturation levels of dissolved gas in acidic or alkaline media are comparable [19–21].

For a perfect zero-gap design, the hydrogen supersaturation at the diaphragm interface should be comparable to the supersaturation at the electrode surface. Yet, since the concentration boundary layer at the electrode surface is relatively thin [1,12], an imperfect zero gap configuration with a small gap can result in a significantly lower supersaturation at the diaphragm interface. To evaluate to what degree the electrode supersaturation extends to the diaphragm interface, it is important to

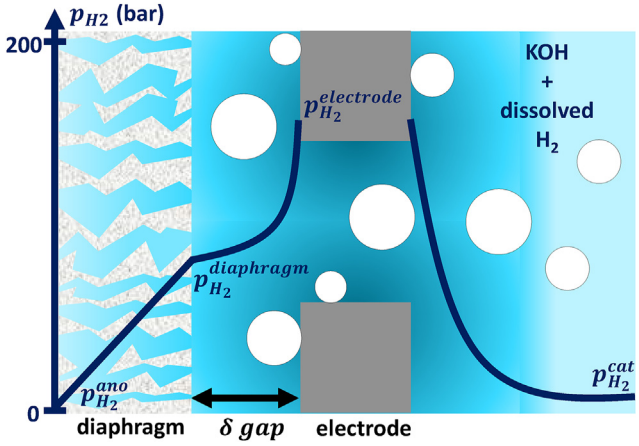

Fig. 1 – Schematic representation of the H_2 concentration profile in an imperfect zero-gap configuration, where $p_{H_2}^{electrode}$ is the H_2 pressure at the electrode surface, $p_{H_2}^{diaphragm}$ is the H_2 pressure at the diaphragm surface and $p_{H_2}^{cat}$ is the pressure in the electrolyte bulk on the cathodic side. At the diaphragm interphase in the anodic side, the H_2 pressure is $p_{H_2}^{ano} \approx 0$.

understand the thickness of the concentration boundary layer at the electrode. In previous work [22] the observed hydrogen crossover in PEM electrolysis was correlated with a mass transfer coefficient in the order of about 10^{-3} m s^{-1}. This would correspond to a concentration boundary layer thickness in the order of 10 μm (considering that hydrogen diffusivity in water is ~10^{-8} m^2 s^{-1}). In other work, in which a dilute alkaline solution was used, a higher concentration boundary layer thickness was reported in the range of 15–170 μm [23].

A key question is how "perfect" the zero gap is in alkaline electrolyzers. The distance between the electrodes is defined not only by the separator thickness, but also by gaskets [24] (and/or O-rings). At industrial scale electrolytic cells generally have a current-carrying area ≥ 1 m^2 and it is difficult to manufacture these large electrodes with high accuracy to obtain an ideal zero gap [5]. It is likely that the electrode is only touching the diaphragm in certain places, but that at other places there can be a gap. Hence, industrial zero-gap electrolyzers are probably imperfect due to the large cell sizes. Also, for laboratory scale alkaline electrolyzers there are currently no commercial well-defined zero-gap alkaline systems available, making it likely that there is also significant variation in gap size for laboratory scale electrolyzers.

Supersaturation levels can be derived from previously reported HTO data for alkaline and PEM [10–13,24]. HTO values of ~0.04–0.15% were reported for current densities in the range of 0.05–0.3 A cm^{-2}, 1 bar, 60–80 °C, ~31% KOH and separated electrolyte circuits using Zirfon Perl UTP 500 as a diaphragm [10,11]. This corresponds to a supersaturation level of ~10 for alkaline medium. In comparison values reported for PEM [11] show supersaturation values in the same order of magnitude as alkaline. Yet, a comparison of supersaturation levels in PEM and AWE electrolyzers cannot be directly made, since PEM has membrane-electrode configurations (using catalyst coated membranes and porous transport layers) that are clearly different from AWE designs, where mesh or perforated electrodes are pushed against a diaphragm.

In this study we further explore how the hydrogen crossover flux depends on the electrode-diaphragm configuration with a special focus on the influence of the gap distance between the electrode and the diaphragm. Therefore, a comparison of finite- and zero-gap AWE designs is made using Zirfon UTP 220 and Zirfon Perl UTP 500. The effect of a finite gap is investigated both at the anodic and cathodic side. Special attention is given to reproducibility, which appears to be a major challenge between different experiments. We carry out experiments at current densities ranging from 0.1 to 0.3 A cm^{-2}, which are representative values for the minimum load of alkaline electrolyzers.

2. Methods

2.1. Electrolysis-cell design

A custom-built electrolysis cell, shown in Fig. 2, was used to conduct the gas crossover measurements. It consists of two polymethyl methacrylate (PMMA) parts in which nickel alloy 201 (Salomon's Metalen) is used as electrode material. Both cathode and anode are fixed using screws on which the power cables can be connected. The nickel electrodes have perforations with a 1-mm hole diameter, an open area of ~40% and a thickness of 0.5 mm. The geometrical area of the electrodes is ~20 cm^2 (~3.5 cm × 5.6 cm). Polytetrafluoroethylene (PTFE) filaments can be inserted below the electrode to create a zero-gap configuration. Additionally, extra PTFE or ethylene-propylene-diene-monomer (EPDM) gaskets can be inserted to create a finite-gap configuration. A Zirfon separator (Agfa®, type UTP Perl 500 or UTP 220) with an effective area of 56 cm^2 is placed between both cell compartments and held in place by an inner EPDM O-ring. An outer O-ring is used to seal the cell. The black inserts shown in Fig. 2 ensure that the gas transport happens primarily through the electrode area and not through the rest of the diaphragm area. Another custom-built electrolysis cell was also used to conduct part of gas crossover measurements. The extra cell was made of polypropylene (PP) with identical design as the original PMMA cell (see Supplementary Information). Due to the similar structural cell configurations, the gas crossover behavior is expected to be comparable.

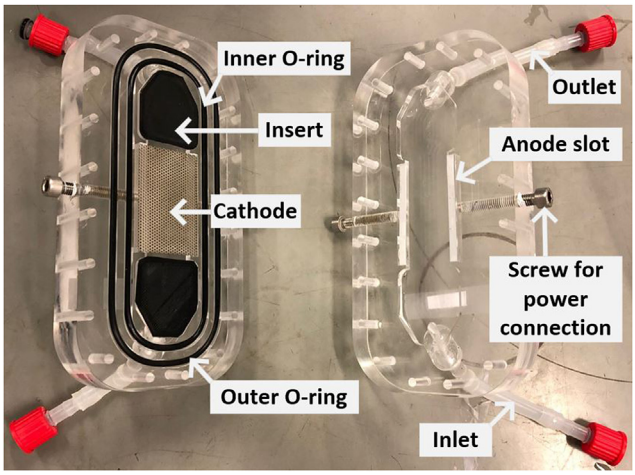

Fig. 2 – Parts of the custom-built electrolysis cell made of PMMA.

2.2. Electrolysis test setup

The overview of the electrolysis test setup is shown in Fig. 3. A power supply (Delta Elektronika model ES030-10) is used to apply the desired current to the electrolysis cell. Both anolyte and catholyte outlet streams of the electrolysis cell are connected to vertical gas-liquid separators. The gas-liquid separators have internal coils that enable heating and cooling of the electrolyte to control the operating temperature of the electrolyzer. In each 300-mL gas-liquid separator the evolved gas products are separated from the electrolyte solution. Both gas streams go through washers at room temperature to remove possible KOH droplets in the gas streams. Subsequently, the O_2 gas stream goes through a hydrophobic membrane (Mitex®, PTFE, pore size of 10 μm) to ensure the removal of any liquid droplets. Then, the O_2 gas stream with traces of H_2 is analyzed in a gas chromatograph (Global Analyser Solutions®) every ~2 min. The gas chromatograph (GC) is equipped with a 5 m long 0.32 mm molecular sieve column for gas separation and a thermal conductivity detector for gas

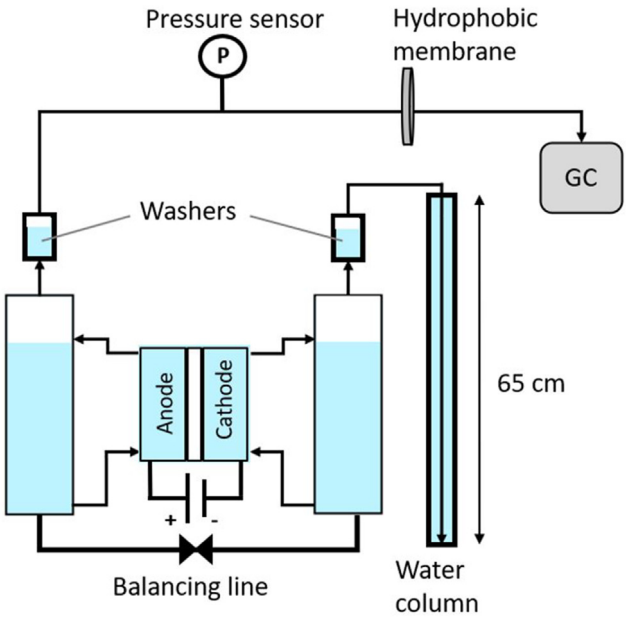

Fig. 3 – Schematic of the AWE test setup applied in this study.

detection. Before the hydrophobic membrane and the GC there is a pressure sensor (Endress + Hauser Cerabar T, pressure range of 0–2 barg) to determine the pressure drop of the gas mixture that flows through the gas analysis line.

The produced hydrogen gas stream flows through a water column in which the liquid height can be manually changed between 0 and 65 cm, to achieve the same pressure drop as measured with the pressure sensor in the O_2 stream. Every time the current is changed the water column level is adjusted accordingly. In this way both electrolysis cell compartments can be operated without a significant differential pressure.

There are no pumps in the test setup to avoid any pressure differentials that could potentially be created by forced convection. Therefore, the recirculation of catholyte and anolyte is only driven by natural convection (induced by bubble motion). Natural convection is also a common approach in industrial electrolysis where flowrates are typically set to maintain the difference between the inlet and outlet temperature of the stack to less than 15 K [25].

The system is operated with separated electrolyte circuits, ensuring that gas crossover only occurs through the separator. A balancing line connects both gas-liquid separators. During experiments this balancing line is closed, but it is opened between measurements for a couple of minutes to avoid the creation of an electrolyte concentration difference between compartments. At the end of every test day, the system is flushed with nitrogen.

2.3. *Diaphragm characterization*

The properties of the diaphragm Zirfon® Perl UTP 500 and the thinner diaphragm (Zirfon® UTP 220) used in this study are given in Table 1. These diaphragms are made of an open mesh polyphenylene sulfide fabric which is symmetrically coated with a mixture of polysulfone and zirconium oxide [26,27]. Zirfon® UTP 220 is thinner and therefore has less ionic resistance compared to Zirfon® Perl UTP 500.

Table 1 – Properties of AWE diaphragms - the Zirfon® Perl UTP 500 and UTP 220 [24,26,27].

Property	PERL UTP 500	UTP 220
Thickness (μm)	500 ± 50	220 ± 30
Porosity (%)	55 ± 10	60 ± 10
Pore size (μm)	0.15 ± 0.05	0.15[a] ± 0.05
Bubble point (bar)	2 ± 1	2 ± 1
Ionic resistance (Ω.cm^2)[b]	0.10	0.05

[a] Assumed to be comparable to UTP 500, as both diaphragms have equivalent bubble points.
[b] At 30 wt% KOH and 80 °C.

The thicknesses of Zirfon PERL UTP 500 and UTP 220 used in the study were determined by measuring it with a digital caliper (Powerfix Profi+, 0.01 mm–150mm). They were measured at four different locations after the diaphragms were soaked in demineralized water for at least 24 h. The measured thicknesses of the diaphragm samples Zirfon PERL UTP 500 and UTP 220 were, respectively, 473 ± 20 μm and 213 ± 20 μm. The presented standard error is the accuracy of the measuring caliper, since the standard deviation for the measurements was smaller than that.

2.4. *Experimental procedure*

The electrolyte with a concentration of 12 ± 1 wt% (2.3 ± 0.3 mol/L) was prepared from KOH pellets (GPR Rectapur VWR Chemicals®). Galvanostatic measurements with an accuracy of ±0.2% of the input current were carried out in the range of 2–6 A, corresponding to a current density range of 0.1–0.3 A cm^{-2}. The stationary gas impurity (hydrogen in oxygen) was measured at 25 ± 3 °C and ambient 1 atm pressure. The electrolysis cell was operated until steady gas impurity levels were observed (up to 90 min). The last 5 measured HTO levels should have a standard deviation < 0.02% to be considered steady state. In the majority of cases the measurements started from high to low current densities, from 0.3 A cm^{-2} with decreasing steps of 0.1 A cm^{-2} until a current density of 0.1 A.cm–2. The majority of the experimental tests were conducted in triplicate to ensure the reproducibility of the results. It is important to point out that the first 5 measured HTO levels of a particular run (first 10 min) should not be considered, due to dead gas volume in the experimental setup and impurities in the sample loop of the gas chromatography.

Besides the experiments at 12 wt% KOH, we have also conducted experiments using different electrolyte concentrations (5, 15 and 27 wt%), diverse diaphragms (Zirfon UTP 500, UTP 220 and UTP 500+) and other electrode-diaphragm gaps. Results of these experiments can be found in the supplementary information.

3. Analysis

3.1. *Gas crossover evaluation*

The stationary anodic gas impurity (HTO) is determined from the measured hydrogen peak area (A_{peak}) in the gas

chromatogram by using equation (1), in which p_{H_2O} is the partial vapor pressure of water.

$$HTO(\%) = \left(2.394 \cdot 10^{-6} \cdot A_{peak} - 0.0097\right) \cdot \frac{1}{1 - p_{H_2O}} \quad (1)$$

The correlation between HTO and the hydrogen permeation flux ($N_{H_2}^{perm}$) is shown in equation (2). The oxygen produced in the anodic compartment (N_{O_2}) in mol cm^{-2} s^{-1} is a function of the applied current density (i) and can be calculated according to equation (3), where, F is the Faraday constant. Combining equations (1) and (2) results in equation (4) for the hydrogen permeation flux ($N_{H_2}^{perm}$) in mol cm^{-2} s^{-1}.

$$HTO(\%) = \frac{N_{H_2}^{perm}}{N_{O_2} + N_{H_2}^{perm}} * 100 \quad (2)$$

$$N_{O_2} = \frac{i}{4 \cdot F} \quad (3)$$

$$N_{H_2}^{perm} = \frac{i \cdot A_{electrode}}{4 \cdot F} \frac{HTO(\%)}{100 - HTO(\%)} \frac{1}{A_{diaphragm}} \quad (4)$$

$A_{electrode}$ is the geometrical area of the electrode and $A_{diaphragm}$ is the diaphragm surface area. As only the diaphragm area next to the electrode area is subjected to high levels of supersaturation, it is assumed that the hydrogen transport through the remaining diaphragm area can be neglected and that hence the electrode area is equal to the diaphragm area. Therefore, equation (3) can be rewritten as equation (5):

$$N_{H_2}^{perm} = \frac{i}{4 \cdot F} \frac{HTO(\%)}{100 - HTO(\%)} \quad (5)$$

The standard deviation (SD) represents the prevailing metric for data dispersion. SD is employed to indicate the variability of each measured HTO percentage (HTO_i) surrounding the HTO mean ($\overline{HTO}$) for a number N of experimental trials. Equation (6) presents the calculation for the standard deviation. The standard deviation of the hydrogen permeation flux can be calculated based on the HTO standard deviation by error propagation.

$$SD = \sqrt{\frac{\sum_{i=1}^{i=N} (HTO_i - \overline{HTO})^2}{N - 1}} \quad (6)$$

As previously stated in this paper, for electrolyzers operated at well balanced pressures and low electrolyte flow rates, hydrogen crossover is primarily driven by diffusion. That means that the hydrogen permeation flux ($N_{H_2}^{perm}$) [8,10,11] can be written as a function of the hydrogen partial pressure at the catholyte diaphragm interface ($p_{H_2}^{diaphragm}$), as shown in equation (7).

$$N_{H_2}^{diff} = \frac{D_{H_2}}{N_M} \cdot S_{H_2} \cdot \frac{p_{H_2}^{diaphragm}}{\delta_{diaphragm}} \quad (7)$$

For a porous diaphragm, the effective diffusion coefficient within the diaphragm can be obtained by correction of the diffusion coefficient in the free electrolyte (D_{H_2}) with the MacMullin number (N_M). The MacMullin number represents the ratio of the tortuosity factor to the porosity of the diaphragm. The MacMullin number is also utilized in the context of resistance, where it indicates the ratio between the resistivity of the diaphragm and the resistivity of the pure electrolyte [6,28,29]. Similarly, it can be applied to diffusive transport within a porous medium. Equation (7) is also a function of the hydrogen solubility in the electrolyte (S_{H_2}) and the diaphragm thickness ($\delta_{diaphragm}$). The higher the amount of dissolved hydrogen in the electrolyte, the higher the hydrogen permeation flux. In contrast, the thicker the diaphragm, the lower the permeation flux. Comparing both diaphragms used in this study, i.e. Zirfon UTP 220 and UTP 500, higher H_2 crossover fluxes are expected for UTP 220 than for UTP 500, due to the smaller thickness of UTP 220.

3.2. Supersaturation evaluation

The hydrogen permeation flux described by equation (5) is equal to the diffusional hydrogen flux defined in equation (7) under the assumption that diffusion is the dominant crossover mechanism. Hence, equation (7) can be rewritten to calculate the hydrogen partial pressure ($p_{H_2}^{diaphragm}$) from the estimated hydrogen permeation flux, resulting in equation (8).

$$p_{H_2}^{diaphragm} = N_{H_2}^{perm} \cdot \frac{N_M \cdot \delta_{diaphragm}}{D_{H_2} \cdot S_{H_2}} \quad (8)$$

The hydrogen supersaturation at the diaphragm surface ($\phi_{H_2}^{diaphragm}$) is the ratio between the concentration of the dissolved gas and the hydrogen equilibrium solubility and is estimated by equation (10). At equilibrium, the hydrogen pressure ($p_{H_2}^{eq}$) is defined by equation (9), assuming that the hydrogen is saturated with water vapor. Therefore, the hydrogen equilibrium pressure is the total cathodic pressure (p_{cat}) corrected by the water vapor pressure above the electrolyte solution (p_{H_2O}).

$$p_{H_2}^{eq} = p_{cat} - p_{H_2O} \quad (9)$$

$$\phi_{H_2}^{diaphragm} = N_{H_2}^{perm} \cdot \frac{N_M \cdot \delta_{diaphragm}}{D_{H_2} \cdot S_{H_2} \cdot p_{H_2}^{eq}} \quad (10)$$

From experiments, HTO levels can be calculated using equation (1). However, equations (7) and (10) require input parameters to estimate the stationary anodic gas impurity, the hydrogen permeation flux and the hydrogen supersaturation at the diaphragm surface. The relevant parameters are summarized in Table 2. The MacMullin numbers were estimated by considering the ohmic resistance data obtained from AGFA® [26] and KOH conductivities measured by Gilliam et al. [30] (see Supplementary information). The molecular diffusion coefficient (D_{H_2}) and the hydrogen solubility (S_{H_2}) were obtained from the data provided by Tham et al. [31] and Ruetschi et al. [32]. The empirical correlation used to estimate the water vapor pressure above a KOH solution (p_{H_2O}) was proposed by Balej [33].

3.3. Gas crossover model

A correlation to estimate the hydrogen pressure at the diaphragm interface ($p_{H_2}^{diaphragm}$) was proposed by de Groot et al.

Table 2 – Relevant parameters to calculate $N_{H_2}^{perm}$ and $\phi_{H_2}^{diaphragm}$

Parameter	Value	Unit
N_M (UTP Perl 500)	3.4	–
N_M (UTP 220)	3.1	–
D_{H_2} [a]	$2.5 \cdot 10^{-9}$	$m^2\ s^{-1}$
S_{H_2} [b]	$3.7 \cdot 10^{-1}$	$mol\ m^{-3}$
p_{H_2O} [a]	0.028	bar

[a] At 25 °C and 12 wt% KOH.
[b] At 30 °C and 12 wt% KOH.

[6] and is given in equation (11). The correlation was obtained by fitting data points from four distinct studies using a zero-gap electrolyzer design [10–12,24]. The hydrogen pressure at the diaphragm interface was found to be dependent on the square roots of the current density (i) and the total cathodic pressure (p_{cat}). A value of 25.8 was found for the parameter f at 30 wt% KOH. In this study we compare our results to that correlation. We assume that $p_{H_2}^{diaphragm}$ is independent of the electrolyte concentration and temperature and therefore a value of $f = 25.8$ is also used in this study. This assumption is based on the work of Glas et al. [21] in which there was no bubble growth difference in alkaline or acidic medium with different normalities. This assumption still needs to be fully proven to validate the use of a constant fitting parameter to estimate properly the supersaturation level in zero-gap electrolyzers. Equation (11) can be rearranged to obtain the hydrogen supersaturation at the diaphragm surface ($\phi_{H_2}^{diaphragm}$), which is shown in equation (12). The hydrogen supersaturation concentration near the diaphragm is only corrected for a specific electrolyte concentration and temperature by multiplying the supersaturation pressure in equation (11) by the hydrogen solubility.

$$p_{H_2}^{diaphragm} = p_{cat} - p_{H_2O} + f \cdot i^{0.5} \cdot p_{cat}^{0.5} \tag{11}$$

$$\phi_{H_2}^{diaphragm} = 1 + \frac{f}{p_{cat} - p_{H_2O}} \cdot i^{0.5} \cdot p_{cat}^{0.5} \tag{12}$$

4. Results and discussion

4.1. Gas crossover evaluation

4.1.1. Influence of cell design on gas crossover

For a zero-gap design with Zirfon UTP 220 the anodic gas impurity "Hydrogen-To-Oxygen" (HTO) as a function of current density is shown in Fig. 4(a). The HTO level decreases with increasing current density and significantly exceeds the value expected based on equilibrium diffusion, which is in line with previous work [11] and the gas crossover model proposed by De Groot et al. [6]. This confirms that supersaturation is likely to play an important role in gas crossover. However, compared to previous work the HTO values are significantly higher and show a large variation as can be noticed from the large standard deviation bars. This is also reflected in Fig. 4(b), which shows the calculated supersaturation and hydrogen crossover fluxes. Please observe that the calculated supersaturation level and the hydrogen crossover flux are directly related to each other. For instance, in the case of the experimental point at a current density of 0.1 A cm^{-2}, the arrow to the left indicates the degree of supersaturation, while the arrow to the right denotes the H_2 crossover flux in mmol $m^{-2}\ s^{-1}$.

HTO values for a finite-gap (500 μm) configuration are shown in Fig. 5(a) as a function of current density for both Zirfon UTP 220 and UTP 500. Supersaturation and hydrogen crossover flux are given in Fig. 5(b)–(c). For UTP 220 the HTO and supersaturation values are over a factor 10 lower than for the zero-gap configuration. Also, the variation in the HTO and supersaturation values is significantly smaller for the finite-gap configuration than for the zero-gap configuration. Gas crossover values are now much closer to the equilibrium diffusion, although there is still some supersaturation.

Comparing finite-gap cells with Zirfon UTP 220 and UTP 500 it can be seen that H_2 crossover fluxes are higher for UTP 220 than for UTP 500, which is expected due to the smaller thickness of UTP 220, while the other diaphragm properties are comparable. Since the diaphragm thickness is corrected for when calculating the supersaturation, one would expect that the calculated supersaturation values would be comparable for

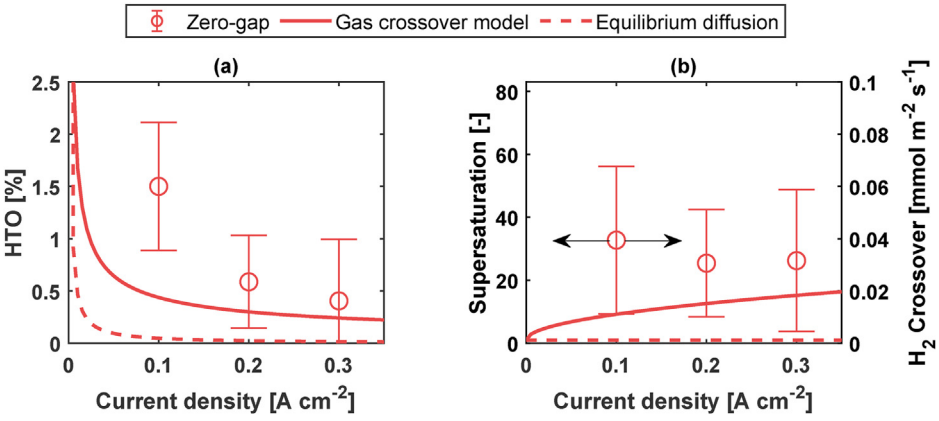

Fig. 4 – (a) Stationary anodic gas impurity (HTO) and (b) calculated H_2 crossover flux and supersaturation as a function of current density for zero-gap. Conditions: 25 °C, 12 wt.% KOH, UTP 220.

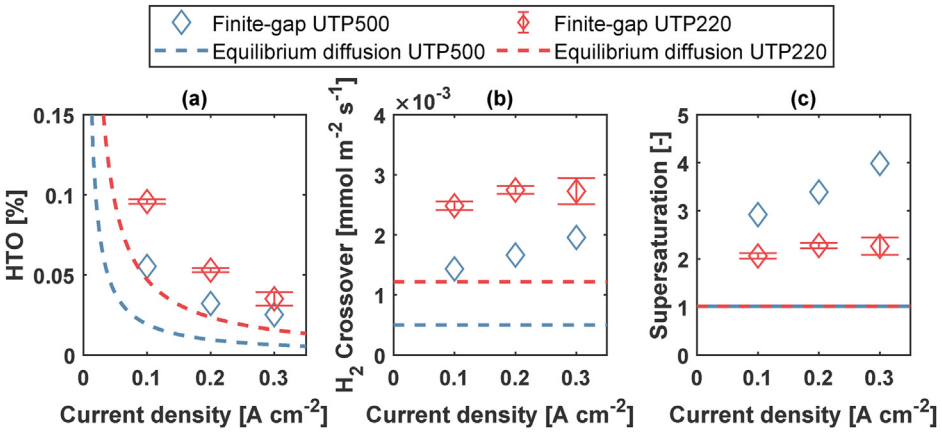

Fig. 5 – (a) Stationary anodic gas impurity (HTO), (b) H_2 crossover flux, and (c) supersaturation as a function of current density for a finite-gap of 500 μm at both cathodic and anodic sides. Conditions: 25 °C, 12 wt.% KOH, Zirfon UTP 500 (blue data) or UTP 220 (red data). (For interpretation of the references to colour in this figure legend, the reader is referred to the Web version of this article.)

both Zirfon diaphragms. However, Fig. 5(c) shows significantly higher supersaturation values for Zirfon UTP 500 (3–4) than for UTP 220 (~2). It is not directly clear why this is. It could be due to small variations in the finite-gap design but might also be due to a possible difference in surface properties of Zirfon UTP 500 compared to UTP 220. Another hypothesis is that a slightly higher supersaturation is estimated due to the assumption that the diaphragm area is equivalent to the electrode geometric area. Crossover could occur in diaphragm areas that do not make full contact with the electrode. Nevertheless, the overall extent of the diaphragm area may have a negligible impact on crossover, as the presence of cell inserts is capable of suppressing gas crossover. Besides, disparities between the two Zirfon diaphragm types cannot be solely attributed to changes in diaphragm area.

4.1.2. *Variation in gas crossover*

To further investigate the large variability in HTO in the zero-gap configuration measurements were performed for a longer time period. Fig. 6 shows results for three different runs with a total operating time of ~270 min for different current densities. There were breaks in between the different runs, but the cell was not opened.

The data show striking changes in HTO during the experiments: in the first run at 0.2 A cm^{-2} the HTO seems to stabilize around ~1% during the first 30 min, but then starts dropping to ~0.3%, where it remains during the rest of the experiment. In contrast, in the third run at 0.3 A cm^{-2} the HTO value seems stable at a low value of ~0.15%, but then suddenly shoots up to ~1%, after which it slowly decreases. In the latter case it was initially believed that the diaphragm was damaged, but there was no visual evidence of any damage when examining the diaphragm. Moreover, a diaphragm damage cannot explain a sudden decrease in HTO as observed in the first run.

The calculated supersaturation near the diaphragm surface during the experiments is given in Fig. 6(b). During the first run at 0.2 A cm^{-2} the supersaturation starts at ~50, but then suddenly drops to ~15. During the second run at 0.1 A cm^{-2} the supersaturation remains low around ~20. In the third run at 0.3 A cm^{-2} the supersaturation starts at a low value of ~10, but then suddenly shoots up to ~80. These results confirm that supersaturation can largely vary even for a cell that remains unopened during an experiment.

The gas-crossover results for a longer time period using a 500 μm-gap are shown in the Supplementary information of this paper. The HTO level fluctuations were not observed anymore, confirming that the gas crossover variation is related to the zero-gap design. For a finite-gap of 500 μm, a supersaturation of ~2 is reached in the range of 0.1–0.3 A cm^{-2}, which is 4-fold lower than the minimum estimated supersaturation when using a zero-gap cell. These supersaturation levels suggests that the gap in the imperfect zero-gap design is lower than 500 μm.

4.1.3. *Influence of the gap side on gas crossover*

The influence of adding a finite-gap only on the anodic or cathodic side on gas crossover is shown in Fig. 7. It can be seen that there is a large difference between a cathode and an anode gap, with the anode gap resulting in much higher HTO values. The values observed for the anode gap are of the same order of magnitude as a zero gap, whereas the values observed for the cathode gap are of the same order of magnitude as the finite gap. In the supplementary information results using a larger cathode gap can be found, which shows that a further increase in gap size on the cathode leads to an even further decrease in HTO levels.

4.1.4. *Limited influence of convection on gas crossover*

5 mbar of overpressure in the cathodic side was created by adding 5 cm of water column in the setup. Therefore a pressure difference was created to promote a convective flux from the cathode to the anode at 0.1 A cm^{-2} (see Supplementary information). A zero-gap at the cathodic side and a gap of 500 μm at anodic side were used in the cell configuration. The HTO level increased slightly from ~0.82% to ~0.88%. This

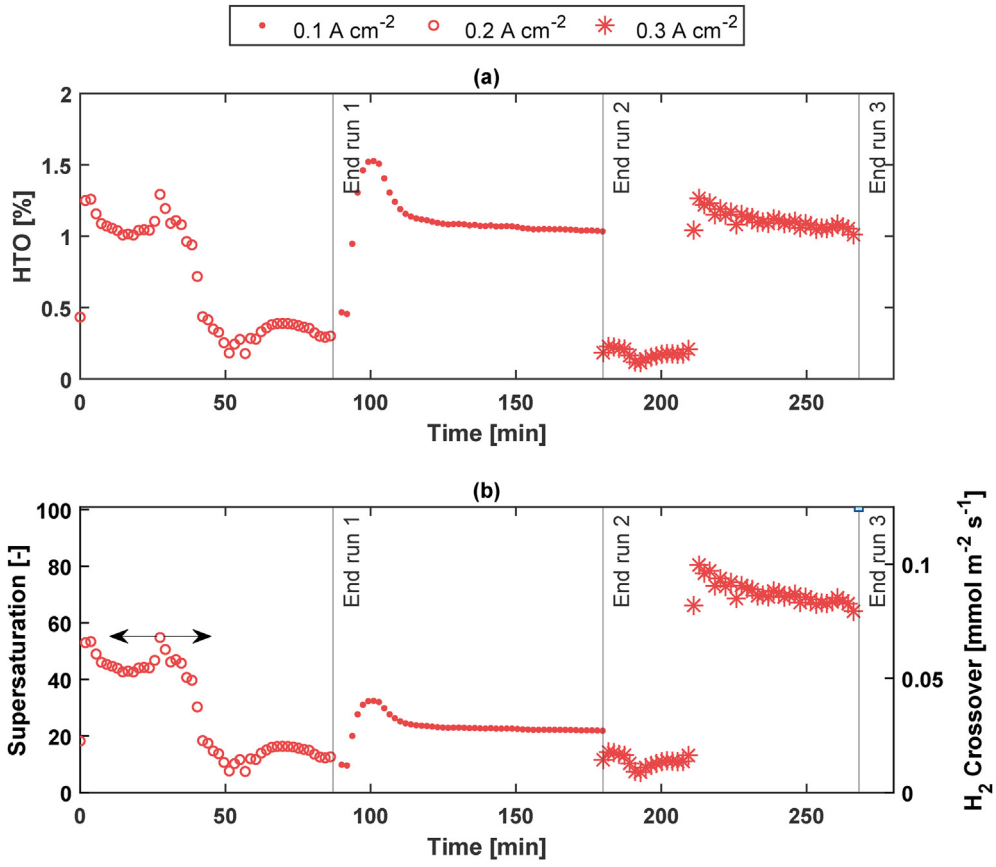

Fig. 6 – (a) Stationary anodic gas impurity (HTO), (b) H_2 supersaturation near the diaphragm surface and H_2 crossover flux as a function of operating time for zero-gap configuration at different non-consecutive current densities, namely 0.2, 0.1 and 0.3 A.cm^{-2}. Conditions: 25 °C, 12 wt.% KOH, Zirfon UTP 220. Note that the experiments at each current density were not performed directly after each other, but included breaks. The time only indicates the real running time.

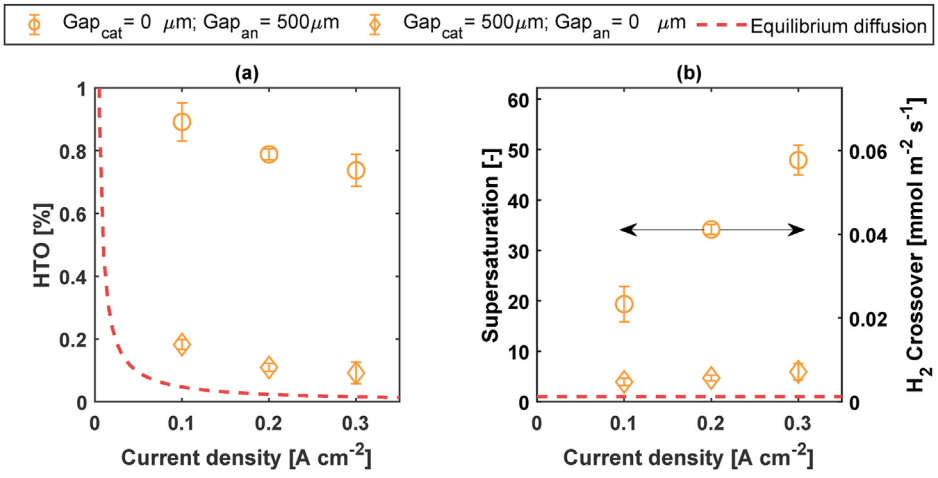

Fig. 7 – (a) Stationary anodic gas impurity (HTO), (b) H_2 crossover flux and supersaturation as a function of current density for finite-gap of 500 μm in the anodic (an) or cathodic (cat) compartments. Conditions: 25 °C, 12 wt.% KOH, Zirfon UTP 220.

shows that convection driven by a pressure difference has a limited influence on gas crossover when there is a zero gap in the cathodic compartment of an electrolyzer. Hence, this confirms that diffusion is the main driver for hydrogen transport through the diaphragm.

4.2. *Discussion about gas crossover in zero-gap electrolyzers*

The results regarding gas crossover in a zero-gap electrolyzer can be rationalized using the scheme depicted in Fig. 1,

especially focusing on the influence of hydrogen supersaturation near the diaphragm surface. The supersaturation levels of ~30 ± 20 are lower than the reported supersaturation at the electrode surface of ~160 at 0.3 A cm^{-2} [15–17]. Yet, the values are higher than supersaturation near the bubble surface of 1.5–20 at 0.01–0.12 A cm^{-2} [15,21]. Therefore, the supersaturation in the diaphragm interface is somewhere in between the supersaturation at the electrode and the equilibrium pressure. The key question is how this supersaturation depends on the diaphragm distance from the electrode or, in other words, how thick is the concentration boundary layer at the cathode surface.

The hydrogen supersaturation still plays a significant role in the bulk concentration hundreds of micrometers from the electrode, which means that the boundary layer is significantly thicker, exceeding the gap size in a close to zero-gap electrolyzer. A study conducted by Janssen et al. [34] provides valuable insights into the mass transfer boundary layer thickness, which is found to be within the range of 10–100 μm when using current densities of 0.01–1.0 A cm^{-2} for hydrogen in acidic and alkaline media. By utilizing the supersaturation levels measured by Shibata [16], assuming their applicability to various electrode and electrolyte types, it is estimated that the Nernst boundary layer thickness at a concentration of 12 wt% KOH and room temperature would fall within the range of ~10–180 μm when operating at current densities of 0.01–1 A cm^{-2} (please refer to the supplementary information for further details). Since especially in the first micrometers within the diffusion layer the supersaturation will show a very strong dependence on distance, a small variation in the "zero-gap" configuration can lead to a large increase or decrease in gas crossover.

Another way to estimate the boundary layer thickness is to determine the mass transfer coefficient in the concentration boundary layer adjacent to the electrode. The global mass transfer coefficient constitutes the combined mass transfer for transport of dissolved products from the electrode towards bubbles and the bulk. The boundary layer thickness is obtained essentially by dividing the molecular diffusivity by the global mass transfer coefficient (suitable for all transported substances including dissolved hydrogen). Due to the intricate interplay of local diffusive and convective phenomena, which are heavily influenced by bubble dynamics, accurately quantifying the overall mass transfer rate in close proximity to the electrode is a challenging task. A couple of authors have reported mass transfer coefficient values for hydrogen evolution in acidic media. Matsushima et al. [35] measured the hydrogen supersaturation in acidic medium and determined mass transfer coefficients in a range of about $5 \cdot 10^{-6} - 5 \cdot 10^{-4}$ m/s depending on the applied current density. Trinke et al. [22] estimated a narrow mass transfer coefficient range of $1.9 \cdot 10^{-3} - 3.2 \cdot 10^{-3}$ m/s at 0.01–1 A cm^{-2} in a PEM electrolyzer. For alkaline electrolysis a higher mass transfer is expected since dissolved hydrogen should be removed from the electrode directly towards the catholyte or hydrogen bubbles. This path has less resistance than in PEM, in which the produced hydrogen has an additional transport resistance through an ionomer layer [22]. On the other hand, it is important to note that the diffusivity of hydrogen in concentrated alkaline solutions is approximately one order of magnitude lower compared to that in pure water used in PEM [22,31], which should lead to a lower mass transfer. Therefore, conducting a direct comparison of mass transfer between PEM and alkaline electrolyzers presents inherent complexities. Besides, there is a disagreement in literature on the mass transfer coefficient values [22,35] and most of data are presented in acidic solution. Therefore, only the values of the boundary layer thickness were used in this study to confirm the hypothesis of the influence of the diaphragm-electrode distance on the local supersaturation.

When using a zero-gap design, the observed fluctuations in supersaturation near the diaphragm surface range between ~8 and 80 as was shown in Fig. 6(b). This alteration is realistic if the cathode-diaphragm gap varies in the order of a couple of microns (within the limits of the concentration boundary layer thickness) due to the imperfect zero-gap configuration. If the diaphragm moves towards the cathode, more supersaturation is present on the diaphragm surface, leading to an increase in the crossover flux. Conversely, if the diaphragm moves slightly away from the cathode, there is less crossover due to reduced supersaturation at the diaphragm surface. Only the cathode-diaphragm gap significantly influences gas crossover, while the diaphragm-anode gap has only shown a limited effect on HTO levels. Conversely, for a finite-gap in which the distance between cathode and diaphragm is hundreds of micrometers, supersaturation levels at the diaphragm interface are relatively low. For example, a supersaturation level of ~2 was observed in our finite-gap electrolyzer using Zirfon UTP 220, as depicted in Fig. 5(c). By comparing the supersaturation levels in a finite- and a zero-gap design it can be concluded that the gap in the imperfect zero-gap design is lower than 500 μm. Yet, it could be in the order of hundred microns when facing a supersaturation level of ~8.

A 5-mbar pressure difference between cathodic and anodic compartments did not significantly increase HTO level. This experiment demonstrated that convection has limited influence on gas crossover with a zero-gap configuration. A higher-pressure difference than 5 mbar is not realistic due to the resulting large water column in the gas-liquid separator.

The hypothesis of diaphragm rupture as an explanation for HTO variations was also dismissed. Visual examination showed no signs of damage. HTO percentage decreased during analysis, contradicting the presence of a diaphragm puncture (Fig. 6(a)). Yet, the hypothesis of an "imperfect" zero-gap assembly remains a valid explanation for such fluctuations. It is rational that the relatively open cell design of alkaline cells (open flow channels, rips to keep electrodes in place) makes the gap in a zero-gap cell unlikely to be zero everywhere. Probably the electrode touches the diaphragm at some points, but at most points there will be some distance between electrode and diaphragm. The electrode design (perforated plate, expanded metal, mesh etc.) inherently hinders the perfect contact with the diaphragm throughout its surface. As a result, the degree of supersaturation will differ across the diaphragm interface, leading to measurements that reflect an averaged supersaturation value. Consequently, usually it is assumed that there is a small diaphragm-electrode gap in scientific papers. De Groot & Vreman [28] have used a value of 50 μm for simulating current distribution in an imperfect zero-gap configuration. Brauns et al. [24] estimated a 250-μm gap.

The HTO fluctuations in the zero-gap electrolyzer observed in this research suggests that the gas crossover depends on the cell design. These results deviate from previous studies [10–12,24], where crossover seemed to be relatively constant and well defined for a zero-gap cell. Yet, the same previous studies have not reported the standard deviation from their data. Therefore, variations in HTO levels could still be present, but not reported. Additionally, almost all the literature data come from the same scientific group [10,11,24] and hence, possibly used the same or comparable cell designs. Contrarily, the experimental data for HTO values from the study of Lee et al. [12], that uses a different zero-gap cell design, are around 2-fold higher then the other datasets [10,11,24]. The impact of small dimensional variations in the cell assembly in the zero-gap design also reflects in the gas crossover model proposed by de Groot et al. [6], which suggested that supersaturation levels can be accurately calculated for a zero-gap configuration. The correlation to estimate supersaturation levels [6] was obtained by fitting data points from four distinct studies [10–12,24], but the data of Lee et al. [12] is underpredicted by this gas crossover model, and so are the HTO levels shown in this study (see Fig. 4). Hence, the correlation is not necessarily representative of all "zero-gap" electrolyzers in literature. Precise cell design with accurately defined zero gap is essential to ensure consistent and reproducible performance, minimizing potential variations in hydrogen supersaturation and in HTO.

Our work potentially opens the way to more flexible alkaline water electrolyzers. While alkaline electrolysis stands as one of the more cost-effective means for green hydrogen production, its lack of flexibility is regarded as a limitation for integration with variable renewable electricity [6]. Our work shows that establishing a relatively narrow cathode-diaphragm gap can reduce gas crossover, particularly at lower current densities. In turn, this reduces the minimum load of the electrolyzer. It is important that this relatively small gap does not result in a much higher electrolyte resistance, since this would reduce the nominal load of the electrolyzer. However, given the high conductivity of the 30 wt% KOH typically used as electrolyte in alkaline electrolyzers, a small gap of up to 500 μm only results in a limited increase in the ohmic resistance. Hence, with the narrow gap it seems possible to maintain a high nominal load, while significantly reducing the minimum load, in this way broadening the load operating window of alkaline electrolyzers.

5. Conclusion

This study shows that the hydrogen crossover in zero-gap alkaline electrolyzers is strongly dependent on the cathode-diaphragm gap. The results confirm that supersaturation at the diaphragm surface is of key importance. Small variations in the gap between the cathode and the diaphragm can have a very large impact on the hydrogen crossover. There is a large variation in the obtained HTO data, most likely as a result of imperfections in the zero-gap design. This observation potentially has significant implications for the operational window of alkaline electrolyzers, as it seems possible to change the gas crossover and hence the minimum load of the electrolyzer. The findings emphasize the importance of optimization of the cathode-diaphragm gap to suppress crossover, leading to enhanced electrolyzer performance. This implies that it should be possible to make alkaline electrolyzers that have a higher flexibility. Based on our results, it seems feasible to introduce a relatively narrow gap in the order of 100 μm that significantly suppresses gas crossover without leading to significantly higher resistance, paving the way to a high current density alkaline electrolyzer with a large operating window.

CRediT authorship contribution statement

Rodrigo Lira Garcia Barros: Conceptualization, Methodology, Formal Analysis, Investigation, Resources, Data Curation, Writing – Original Draft, Writing – Review & Editing, Visualization, Supervision. **Joost T. Kraakman:** Conceptualization, Methodology, Formal Analysis, Investigation, Data Curation, Writing – Review & Editing. **Carlijn Sebregts:** Conceptualization, Methodology, Formal Analysis, Investigation, Data Curation. **John van der Schaaf:** Conceptualization, Supervision, Project administration. **Matheus T. de Groot:** Conceptualization, Methodology, Resources, Writing – Original Draft, Writing – Review & Editing, Supervision, Project administration, Funding acquisition.

Data availability

The data is available on Mendeley data repository under the DOI: 10.17632/kndwxjhdpr.1.

Declaration of competing interest

The authors declare that they have no known competing financial interests or personal relationships that could have appeared to influence the work reported in this paper.

Acknowledgments

The authors thankfully acknowledge the Topsector Energie funding by the Netherlands Enterprise Agency (project TWAS118004).

Appendix A. Supplementary data

Supplementary data to this article can be found online at https://doi.org/10.1016/j.ijhydene.2023.09.280.

REFERENCES

[1] Lopata JS, Kang SG, Cho HS, Kim CH, Weidner JW, Shimpalee S. Investigating influence of geometry and operating conditions on local current, concentration, and crossover in alkaline water electrolysis using computational fluid dynamics. Electrochim Acta Sep. 2021;390. https://doi.org/10.1016/j.electacta.2021.138802.

[2] Brauns J, Turek T. Alkaline water electrolysis powered by renewable energy: a review. In: Processes, 8. MDPI AG; Feb. 01, 2020. https://doi.org/10.3390/pr8020248.
[3] IRENA. Geopolitics of the energy transformation : the hydrogen factor. Abu Dhabi: IRENA; 2022.
[4] International Renewable Energy Agency. Green hydrogen cost reduction: scaling up electrolysers to meet the 1.5°C climate goal. Abu Dhabi. 2020 [Online]. Available: www.irena.org/publications.
[5] Yasuhide N, Yousuke U, Keiji M. Bipolar alkaline water electrolysis unit and electrolytic cell. WO2013191140A1; 2013.
[6] de Groot MT, Kraakman J, Lira Garcia Barros R. Optimal operating parameters for advanced alkaline water electrolysis. Int J Hydrogen Energy Sep. 2022;47(82):34773–83. https://doi.org/10.1016/j.ijhydene.2022.08.075.
[7] Schmidt O, Gambhir A, Staffell I, Hawkes A, Nelson J, Few S. Future cost and performance of water electrolysis: an expert elicitation study. Int J Hydrogen Energy Dec. 2017;42(52):30470–92. https://doi.org/10.1016/j.ijhydene.2017.10.045.
[8] Li Y, et al. Active pressure and flow rate control of alkaline water electrolyzer based on wind power prediction and 100% energy utilization in off-grid wind-hydrogen coupling system. Appl Energy Dec. 2022;328. https://doi.org/10.1016/j.apenergy.2022.120172.
[9] Haverkort JW, Rajaei H. Electro-osmotic flow and the limiting current in alkaline water electrolysis. Journal of Power Sources Advances Dec. 2020;6. https://doi.org/10.1016/j.powera.2020.100034.
[10] Haug P, Koj M, Turek T. Influence of process conditions on gas purity in alkaline water electrolysis. Int J Hydrogen Energy Apr. 2017;42(15):9406–18. https://doi.org/10.1016/j.ijhydene.2016.12.111.
[11] Trinke P, Haug P, Brauns J, Bensmann B, Hanke-Rauschenbach R, Turek T. Hydrogen crossover in PEM and alkaline water electrolysis: mechanisms, direct comparison and mitigation strategies. J Electrochem Soc 2018;165(7):F502–13. https://doi.org/10.1149/2.0541807jes.
[12] Lee HI, et al. Advanced Zirfon-type porous separator for a high-rate alkaline electrolyser operating in a dynamic mode. J Membr Sci Dec. 2020;616. https://doi.org/10.1016/j.memsci.2020.118541.
[13] Bernt M, Schröter J, Möckl M, Gasteiger HA. Analysis of gas permeation phenomena in a PEM water electrolyzer operated at high pressure and high current density. J Electrochem Soc Jan. 2020;167(12):124502. https://doi.org/10.1149/1945-7111/abaa68.
[14] PERIC. Technical parameters - alkaline type hydrogen generator - PERIC. 2023. http://www.peric718.com/Alkaline-Type-Hydrogen-G/r-86.html. [Accessed 5 June 2023].
[15] Vogt H. On the supersaturation of gas in the concentration boundary layer of gas evolving electrodes. Electrochim Acta 1980;25(5). https://doi.org/10.1016/0013-4686(80)87052-6.
[16] Shibata S. The concentration of molecular hydrogen on the platinum cathode. Bull. chem. Soc. Japan Jan. 1963;36(1):53–7.
[17] Shibata S. Supersolubility of hydrogen in acidic solution in the vicinity of hydrogen-evolving platinum cathodes in different surface states. Denki Kagaku Oyobi Kogyo Butsuri Kagaku 1976;44(11):709–12.
[18] Vogt H. The quantities affecting the bubble coverage of gas-evolving electrodes. Electrochim Acta 2017;235. https://doi.org/10.1016/j.electacta.2017.03.116.
[19] Tawfik ME. 'Maximizing fluid delivered by bubble free electroosmotic pump', PhD thesis. New Brunswick: The State University of New Jersey; 2017.
[20] Tawfik ME, Diez FJ. On the relation between onset of bubble nucleation and gas supersaturation concentration. Electrochim Acta 2014;146. https://doi.org/10.1016/j.electacta.2014.08.147.
[21] Glas JP, Westwater JW. Measurements of the growth of electrolytic bubbles. Int J Heat Mass Tran 1964;7(12):1427–43.
[22] Trinke P, Bensmann B, Hanke-Rauschenbach R. Current density effect on hydrogen permeation in PEM water electrolyzers. Int J Hydrogen Energy May 2017;42(21):14355–66. https://doi.org/10.1016/j.ijhydene.2017.03.231.
[23] Ando K, Uchimoto Y, Nakajima T. Concentration profile of dissolved gas during hydrogen gas evolution: an optical approach. Chem Commun Nov. 2020;56(92):14483–6. https://doi.org/10.1039/d0cc05695b.
[24] Brauns J, et al. Evaluation of diaphragms and membranes as separators for alkaline water electrolysis. J Electrochem Soc Jan. 2021;168(1):014510. https://doi.org/10.1149/1945-7111/abda57.
[25] De Nora. De nora electrodic package for alkaline water electrolysis. 2020.
[26] Agfa-Gevaert NV. Technical data sheet: Zirfon UTP 220. May 2021.
[27] Agfa-Gevaert NV. Technical data sheet: Zirfon Perl UTP 500. May 2020.
[28] de Groot MT, Vreman AW. Ohmic resistance in zero gap alkaline electrolysis with a Zirfon diaphragm. Electrochim Acta Feb. 2021;369. https://doi.org/10.1016/j.electacta.2020.137684.
[29] Tjaden B, Brett DJL, Shearing PR. Tortuosity in electrochemical devices: a review of calculation approaches. In: International materials reviews, 63. Taylor and Francis Ltd.; Feb. 17, 2018. p. 47–67. https://doi.org/10.1080/09506608.2016.1249995.
[30] Gilliam RJ, Graydon JW, Kirk DW, Thorpe SJ. A review of specific conductivities of potassium hydroxide solutions for various concentrations and temperatures. Int J Hydrogen Energy Mar. 2007;32(3):359–64. https://doi.org/10.1016/j.ijhydene.2006.10.062.
[31] Tham MK, Walker RD, Gubbins KE. Diffusion of oxygen and hydrogen in aqueous potassium hydroxide solutions. J Phys Chem 1970;74(8). https://doi.org/10.1021/j100703a015.
[32] Ruetschi P, Amlie RF. Solubility of hydrogen in potassium hydroxide and sulfuric acid. Salting-Out and hydration. J Phys Chem 1966;70(3):718–23 [Online]. Available: https://pubs.acs.org/sharingguidelines.
[33] Balej J. Water vapour partial pressures and water activities in potassium and sodium hydroxide solutions over wide concentration and temperature ranges. 1985.
[34] Janssen LJJ, Hoogland JG. The effect of electrolytically evolved gas bubbles on the thickness of the diffusion layer - II. Pergamon Press; 1973.
[35] Matsushima H, Kiuchi D, Fukunaka Y. Measurement of dissolved hydrogen supersaturation during water electrolysis in a magnetic field. Electrochim Acta Oct. 2009;54(24):5858–62. https://doi.org/10.1016/j.electacta.2009.05.044.